

CrossMark
click for updatesCite this: *Soft Matter*, 2015, 11, 2251

Atomistic simulations of the structure of highly crosslinked sulfonated poly(styrene-co-divinylbenzene) ion exchange resins

 María A. Pérez-Maciá,^a David Curcó,^{*a} Roger Bringué,^a Montserrat Iborra^a
and Carlos Alemán^{*bc}

The microscopic structures of highly crosslinked sulfonated poly(styrene-co-divinylbenzene) resins have been modeled by generating atomistic microstructures using stochastic-like algorithms, which are subsequently relaxed using molecular dynamics. Two different generation algorithms have been tested. The relaxation of the microstructures generated by the first algorithm, which is based on a homogeneous construction of the resin, leads to a significant overestimation of the experimental density as well as to an unsatisfactory description of the porosity. In contrast, the generation approach that combines algorithms for the heterogeneous growing and branching of the chains enables the formation of crosslinks with different topologies. In particular, the intrinsic heterogeneity observed in these resins is efficiently reproduced when the topological loops, which are defined by two or more crosslinks closing a cycle, are present in their microscopic description. Thus, the apparent density, porosity and pore volume estimated using microstructures with these topological loops, called *super-crosslinks*, are in very good agreement with the experimental results. Although the backbone dihedral angle distribution of the generated and relaxed models is not influenced by the topology, the number and type of crosslinks affect the medium- and long-range atomic disposition of the backbone atoms and the distribution of sulfonic groups. An analysis of the distribution of the local density indicates that super-crosslinks are responsible for the *heterogeneous homogenization* observed during the MD relaxation. Finally the π - π stacking interactions have been analyzed. Results indicate that those in which the two rings adopt a T-shaped disposition are considerably more abundant as compared to those with the co-facially oriented rings, independently of the resin topology.

Received 1st November 2014
Accepted 16th January 2015

DOI: 10.1039/c4sm02417f

www.rsc.org/softmatter

Introduction

Polymeric resins based on styrene-divinylbenzene, P(S-DVB), are currently used in many industrial processes, for example, waste water treatments (*i.e.* removal of organic pollutants, removal of toxic metals, ions exchange processes),¹⁻⁵ hydrogen storage,^{6,7} hydrometallurgy,⁸ chromatography^{9,10} and separation of biomolecules.^{11,12} In addition, the utilization of P(S-DVB) resins as a catalyst in a number of industrial processes is also quite important, as they offer potentially much higher capacity for the supported functionality than conventional inorganic carriers.¹³⁻¹⁹ Thus, many key large-scale chemical processes have been established employing sulfonic acid resins as a

catalyst. These include the manufacture of bisphenol A, isopropyl alcohol, alkylated phenols, branched ethers (petrol organic 'anti-knocks') such as methyl *tert*-butyl ether (MTBE), and a variety of alkyl esters including important (meth)acrylate esters.¹⁶⁻¹⁹

The catalytic performance of ion exchange catalysts depends critically on both the nano-environment surrounding the active centers and their accessibility. The accessibility of the active centers in these materials is dramatically affected by the extent of swelling of the polymer mass in contact with the reaction medium. Because of the difficulty in experimentally determining the structure of the polymeric resins and the swollen-state morphology, the exploitation of ion-exchange catalysts is still based on a trial and error approach rather than on comprehensive understanding and design of their parameters.

The employment of experimental techniques to get structural information of ion exchange resins is a complex task; therefore, atomistic computer simulations currently represent a distinctive method for answering questions related with the environment and the accessibility of active centers. Within this context, some atomistic computer simulation studies have been

^aDepartament d'Enginyeria Química, Facultat de Química, Universitat de Barcelona, Martí i Franquès 1, Barcelona E-08028, Spain. E-mail: dcurco@ub.edu

^bDepartament d'Enginyeria Química, E.T.S. d'Enginyers Industrials de Barcelona, Universitat Politècnica de Catalunya, Diagonal 647, Barcelona E-08028, Spain. E-mail: carlos.aleman@upc.edu

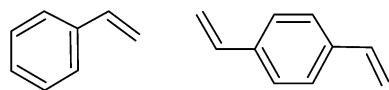
^cCenter for Research in Nano-Engineering, Universitat Politècnica de Catalunya, Campus Sud, Edifici C', C/Pasqual i Vila s/n, Barcelona E-08028, Spain

reported to establish the relationships between the structure and transport phenomena in ion-exchange membranes.^{20–28} However, such studies were essentially focused on the controlled diffusion of small molecules (*e.g.* protons and water) across the membranes rather than on structural aspects for the application of the material in catalysis.

The aim of this paper is to offer a contribution to the understanding of the microscopic structure of ion-exchange P(S-DVB) resins using atomistic computer simulations. For this purpose, different stochastic methodologies are proposed to generate reliable atomistic models of the resins, which have been subsequently relaxed using Molecular Dynamics (MD) simulations. A comparison of the microstructures obtained using such procedures reveals that the topology (*i.e.* number, type and architecture of the crosslinks) dominates the fundamental properties of the examined resins (*i.e.* the apparent density, the porosity and the volume of the pores). Thus, the atomistic description of highly crosslinked sulfonated P(S-DVB) resins requires the specific topological features associated with the so-called “*super-crosslinks*” (see below). After this, the influence of the topology in microscopic properties, for example, the local structure, distribution of sulfonic acid groups and both the frequency and kind of π - π stacking interactions between aromatic phenyl rings, are examined.

Modeled P(S-DVB) resin

P(S-DVB) resins are obtained through the copolymerization of styrene and divinylbenzene monomers (Scheme 1). The resin modeled in this work is highly crosslinked (*i.e.* divinylbenzene content higher than 17 wt%) and functionalized with sulfonic acid. Monosulfonated resins present one sulfonic group per phenyl ring. Table 1 lists the physical properties determined^{29–31} for Amberlyst 15®, which is a highly crosslinked (19–20% w/w) monosulfonated resin, used as a reference in this work to model P(S-DVB).



Scheme 1 Styrene (left) and divinylbenzene (right) monomers.

Construction of the polymer network

The construction of heterogeneously ordered macromolecular multi-chain systems is always a very difficult task because the relatively high density and connectivity of the molecular systems significantly reduce the efficiency of conventional simulation methods.³² Additionally, the construction of P(S-DVB) networks is restricted by the crosslinks formed by the divinylbenzene units. In order to overcome these difficulties, two different procedures have been employed in this work. The first one, hereafter denoted as HGA (*Homogeneous Generation Approach*), is based on the generation of polystyrene segments of identical lengths (*i.e.* same number of repeat copolymerized monomers), while the second approach, called CGA (*Combined Growing Approach*), enables the generation of segments defining the internal loops by combining two growing algorithms. In both these approaches, the following conditions are fulfilled: (1) molecular internal geometry restrictions (*i.e.* bond lengths and bond angles) are satisfied; and (2) atomic overlaps between atoms separated by three or more chemical bonds are completely avoided (*i.e.* interatomic distances are equal or higher than the sum of the van der Waals radii).

Homogeneous generation approach (HGA)

This strategy can be summarized in four main steps (Fig. 1):

(a) **Construction of the first polymer chain.** The styrene monomer is constructed within the simulation box according to its chemical architecture (Fig. 1a). After this, the *ortho*, *meta* or *para* position of the phenyl ring is randomly selected, according to previously defined probabilities, to attach the sulfonic acid group. Next, the position for growing the second styrene unit is randomly chosen between the two available positions (identified as 1 and 2 in Fig. 1b). It should be noted that this selection is related with the chain growing direction. After constructing the second repeat unit, the sulfonic group is attached to its phenyl ring at a position randomly selected among *ortho*, *meta* and *para*. This procedure is repeated until a polymer chain, containing *m* sulfonated styrene units, has been created (Fig. 1c).

(b) **Selection of crosslinking positions.** Among the *m* sulfonated styrene units of the first polymer chains, one is

Table 1 Physical properties of Amberlyst 15® as reported in the literature and determined the authors of this study

Property	Values from the literature	Values obtained by the authors of this study
Sulfur content (wt%)	13.8 ^a	15.02 ± 0.12 ^b
Porosity, θ (%)	31.9 ^a	31.7 ^c
Apparent density, ρ_a (g cm ⁻³)	1.012 ^a	0.97 ^d
Average pore diameter, d_{pore} (nm)	28.8 ^a ; 31.8 ^e	—
Exchange capacity (meq. H ⁺ g ⁻¹)	4.3 ^a	4.81 ^f
DVB content (wt%)	20 ^g	—

^a From ref. 29. ^b Determined by the authors of this study using elemental analysis. ^c Calculated as $\theta = V_g/(V_g + 1/\rho_s)$, where V_g is the pore volume per mass of resin determined by the adsorption of N₂ at 77 K and $P/P_0 = 0.99$ and ρ_s is the skeletal density measured by helium displacement. $V_g = 0.328 \text{ cm}^3 \text{ g}^{-1}$. $\rho_s = 1.416 \text{ g cm}^{-3}$. ^d Indirectly determined using $V_g = 0.328 \text{ cm}^3 \text{ g}^{-1}$. $\rho_s = 1.416 \text{ g cm}^{-3}$. ^e From ref. 30. ^f Determined by titration against a standard base following the procedure described in ref. 31. ^g Information supplied by the manufacturer as mol% of crosslinker used to prepare the network.

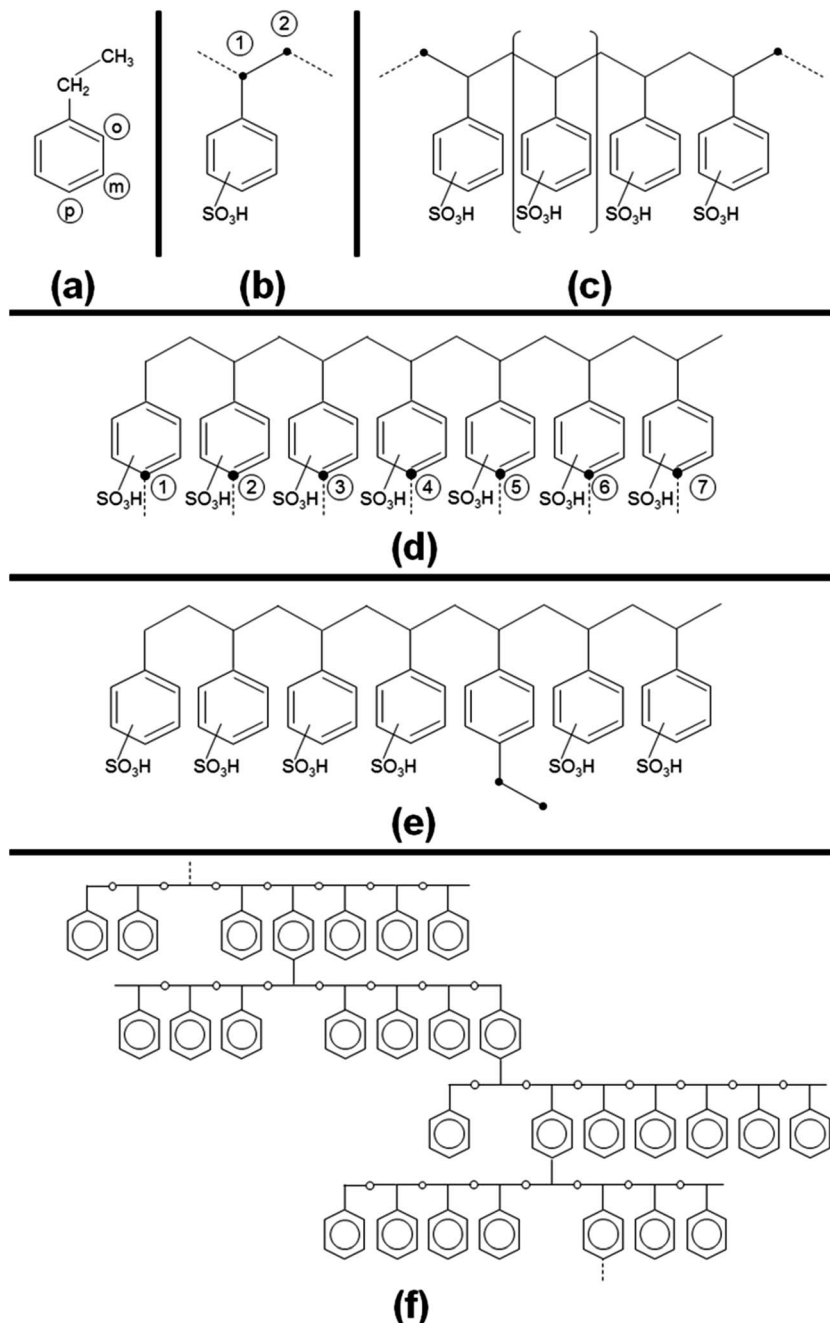


Fig. 1 Schematic representation of the main steps involved in the construction of P(S-DVB) networks using the HGA method: (a) styrene monomer and identification of the possible positions for the sulfonic acid group (*ortho*, *meta* and *para*); (b) available positions (1 and 2) for the growing of the polymer chain by adding the second sulfonated styrene unit; (c) growing of the polymer chain; (d) selection of n crosslink positions from a total of m ; (e) transformation of n sulfonated styrene units into divinylbenzene units; and (f) P(S-DVB) network obtained using the HGA strategy.

randomly selected and transformed, after eliminating its sulfonic acid group, into a divinylbenzene unit (Fig. 1d). In order to keep the styrene/divinylbenzene ratio close to that of the Amberlyst 15® manufacturer specifications, in this work, m was fixed to 7.

(e) Construction of the second polymer chain. The divinylbenzene unit generated in the first chain is used to initiate the growing of the second polymer chain (Fig. 1e). For this purpose, $m - 1$ sulfonated styrene units were built using the procedure

described in (a), one of them being transformed into a divinylbenzene unit as indicated in (b). Accordingly, in addition to the $m - 2$ sulfonated styrene units, the new chain contains two divinylbenzene units: the one coming from the previous chain (which has been used to initiate the growing of this chain) and the one derived from the transformation of styrene into divinylbenzene (which will be used in (d) to initiate the growing of the next chain).

(d) Repetition. The remaining segments are generated using the procedures indicated in (a)–(c). Fig. 1f provides a

schematic representation of the resin network obtained using the HGA method.

In this approach, repeat units are constructed one-by-one. After constructing a repeat unit, the possible existence of steric overlaps with previously generated units is systematically examined. If such interactions are detected, the generation process stops and a new position/unit is randomly selected among the remaining ones. If steric clashes still exist, the process is restarted from the previous step or as many previous steps as necessary (if the clashes persist). On the other hand, the application of this procedure showed that sulfonation typically occurs at the *meta* or, preferentially, *para* positions of the aromatic ring since the *ortho* substitution is sterically hindered.

Combined growing approach (CGA)

The generation of the first sulfonated polystyrene chain is identical for both the HGA and CGA procedures, differences between them starting once a minimal number, r , of sulfonated styrene units have been added to the first chain. After this, the CGA strategy consists of a combination of two different algorithms: the enlargement-crosslinking, which looks for suitable crosslink geometries among the generated sulfonated styrene units and grows the molecule using the existing ends, and the branching algorithm, which is applied every k steps of enlargement-crosslinking and creates new crosslinks increasing the number of ends in the supermolecule.

(a) Enlargement-crosslinking algorithm. Once the r sulfonated styrene unit has been attached to the previous one ($r - 1$), the position for growing the $r + 1$ sulfonated styrene unit is randomly chosen between one of the available ends. At the initial stages, the number of available ends is only two (identified as 1 and 2 in the HGA method, Fig. 1b). However, after combining with the branching algorithm (see below), the number of available ends grows progressively. This feature represents an important difference between the CGA and HGA approaches, since, in the former, the increasing number of available ends enables the construction of polymer segments with different lengths, while the length of all the segments is identical in the latter.

After the construction of the $r + 1$ sulfonated styrene unit, the surrounding of the carbon atom located at the *para* position of the phenyl ring is examined to look for a backbone tertiary carbon atom at a distance similar to that typically found for C–C bonds (*i.e.* bond length with a specified tolerance). If this condition is satisfied, the existence of suitable bond angles (with specified tolerances) is also checked. If these two internal geometry conditions are met, the phenyl group attached to such a tertiary carbon atom and the sulfonic group of the $r + 1$ styrene unit are removed, while a new C–C bond connecting the two units is created. If the conditions are not satisfied, the whole $r + 1$ styrene unit is removed and re-constructed. This reconstruction process is repeated until a successful transformation of styrene into divinylstyrene or until a pre-specified number of trials, s , has been reached. In the latter case, the sulfonated styrene monomer is maintained. Once the crosslinking degree has reached a pre-defined value (*i.e.* in this work,

this value corresponds to the one experimentally observed), the crosslinking algorithm becomes inactive and the structure only grows at the available ends.

Fig. 2a provides a schematic representation of this algorithm. More specifically, two possible locations at one of the ends for the new sulfonated styrene units are displayed. As it can be seen, position 1 does not satisfy the internal geometry restrictions to transform sulfonated styrene into divinylbenzene, while position 2 satisfies this criterion. This procedure allows the formation of crosslinks in a supermolecule that grows heterogeneously.

(b) Branching algorithm. Application of the enlargement-crosslinking algorithm is not enough to construct a P(S-DVB) resin with the physical characteristics described in Table 1. Accordingly, such algorithm has been combined with the branching algorithm, which is applied after a previously specified number of repeat units, k , has been generated. In the branching algorithm, a carbon atom located at the *para* position of the phenyl ring is randomly selected among all the sulfonated styrene units contained in the simulation box. Then, the sulfonic group is removed and the styrene unit is transformed into a divinylbenzene unit. This strategy results in the generation of two new end positions to grow the polymer chain, as schematically represented in Fig. 2b.

Simulation details

All the MD simulations were performed using the GROMACS 4.6.5 program.³³ The energy was calculated using the following force-field expression:

$$\begin{aligned}
 V = & \frac{1}{2} \sum_{\text{bonds}} k_b (b - b_0)^2 + \frac{1}{2} \sum_{\text{angles}} k_\theta (\theta - \theta_0)^2 + \sum_{\text{dihedrals}} k_\phi (1 \\
 & + \cos(n\phi - \phi_0)) + \sum_{\text{non-bonded}} 4\epsilon_{ij} \left(\left(\frac{\sigma_{ij}}{r_{ij}} \right)^{12} - \left(\frac{\sigma_{ij}}{r_{ij}} \right)^6 \right) \\
 & + \frac{q_i q_j}{4\pi\epsilon_0\epsilon_r r_{ij}}
 \end{aligned} \quad (1)$$

where the first two sums represent the harmonic approximation for stretching and bending contributions, followed by a Fourier series expansion for the torsional term. In these bonding terms, k_b , k_θ and k_ϕ are the bond, angle and dihedral angle force constants, respectively; b , θ and ϕ are the bond length, bond angle and dihedral angle, respectively; and the subindex zero represents the equilibrium values for such geometric parameters. The second part of expression (1) contains the non-bonding interactions, which are represented by the sum of Coulomb and 6–12 Lennard-Jones terms. In these contributions, ϵ_{ij} is the depth of the potential well for the interaction of atoms i and j , σ_{ij} is the distance where the Lennard-Jones potential is exactly zero, q_i is the partial atomic charge of atom i , ϵ_0 is the electric constant, ϵ_r is the effective dielectric constant and r_{ij} is the distance separating atoms i and j . The Lennard-Jones parameters between the pairs of different atoms are obtained from the Lorentz–Berthelot mixing rules, in which ϵ_{ij} values are based on the geometric mean of ϵ_i and ϵ_j and σ_{ij} values are based on the arithmetic mean of σ_i and σ_j . For 1–4

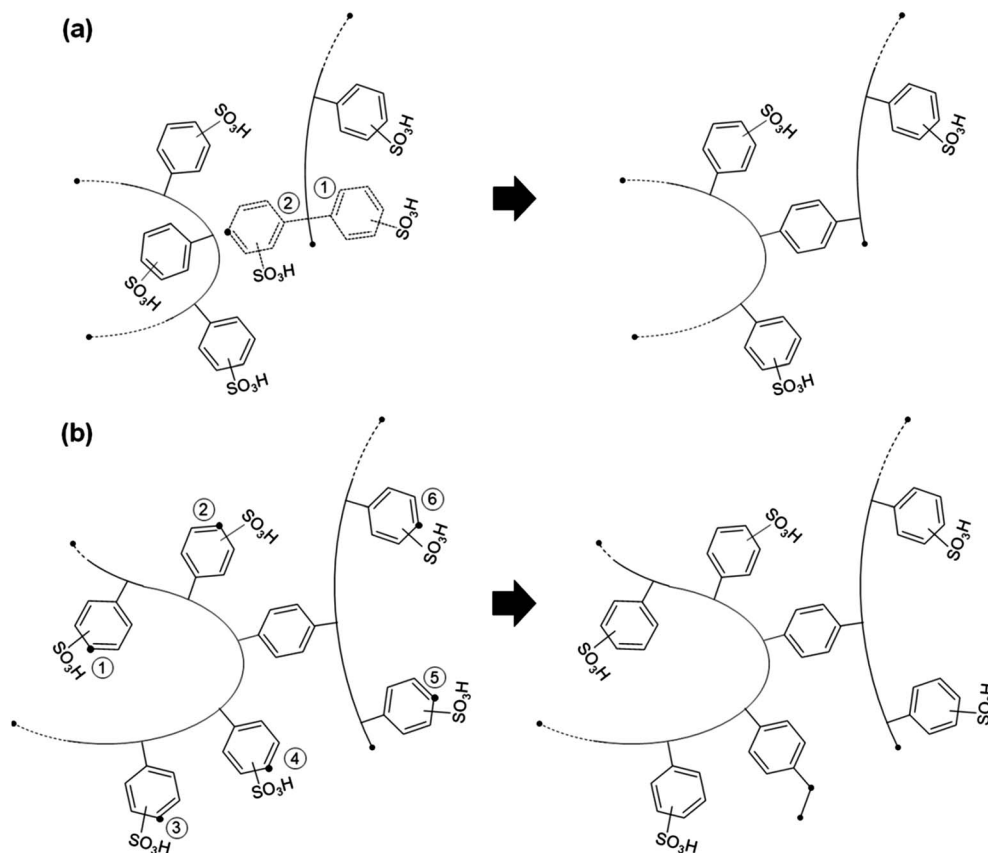


Fig. 2 Application of the two algorithms involved in the CGA method: (a) the enlargement-crosslinking algorithm is illustrated through the selection of position 2 for the formation of a new crosslink; and (b) the branching algorithm is applied by randomly choosing the *para* carbon atom 4 (among a total of 6) to remove the sulfonic acid group and transform the sulfonated styrene unit into divinylbenzene, resulting in the creation of two new ends.

interactions (those between atoms separated by three chemical bonds), the strength of the Lennard-Jones and electrostatic interactions were scaled down by a factor of 0.5 and 0.8333, respectively.

Stretching, bending, torsional and van der Waals force field parameters were extracted from the general AMBER force field (GAFF).³³ Atomic charges were computed at the HF/6-31G(d) level using the Restrained ElectroStatic Potential (RESP) strategy.³⁴ Charges, which were calculated on different model molecules, were scaled ($c = 0.71$) to reflect that the polarization in condensed media is smaller than in the gas-phase.^{35,36} Fig. 3 provides the atomic charges used in this work to represent the electrostatic interactions involving styrene, sulfonated styrene and divinylbenzene units.

Periodic boundary conditions were applied using the nearest image convention. Newton's equations of motion were integrated using the leap-frog algorithm using a numerical integration step of 1 fs. An atom pair distance cut-off of 14.0 Å was applied to compute the van der Waals interactions. Beyond such a cut off distance, electrostatic interactions were calculated by using Particle Mesh Ewald method, with a points grid density of the reciprocal space of 1 Å³.³⁷ The Noose-Hoover thermostat^{38,39} was used with a relaxation time of 0.5 ps. The Parrinello-Rahman⁴⁰ barostat

was used to keep the pressure at 1 atm, the oscillation period being set at 1 ps.

Before MD trajectories, all the generated P(S-DBV) microstructures were submitted to 5000 steps of energy minimization using the steepest descent method. Next, configurations were heated up to 300 K during 500 ps in a NVT-MD simulation. After this, 500 ps at 298 K of NVT-MD were run. Finally, 500 ps NPT-MD were run for density relaxation with a pressure of 1 atm. For each microstructure, the last snapshot of the last NPT-run was the starting point for NPT-MD productive trajectories; the production time ranged from 30 to more than 60 ns.

Results and discussion

Topology-density relationship

Crosslinked networks have been modeled by several authors. For example, Doherty and co-workers⁴¹ created poly(methyl acrylate) networks using lattice-based simulations using the polymerization MD scheme. Yarovsky *et al.*⁴² have presented a methodology to cross-link low molecular weight water-soluble phosphate-modified epoxy resins. More recently, Gou *et al.*⁴³ and Fan *et al.*⁴⁴ built cross-linked networks for epoxy resins (EPON-862) using Accelrys simulation package.⁴⁵ However, no details were provided in such studies regarding the cross-

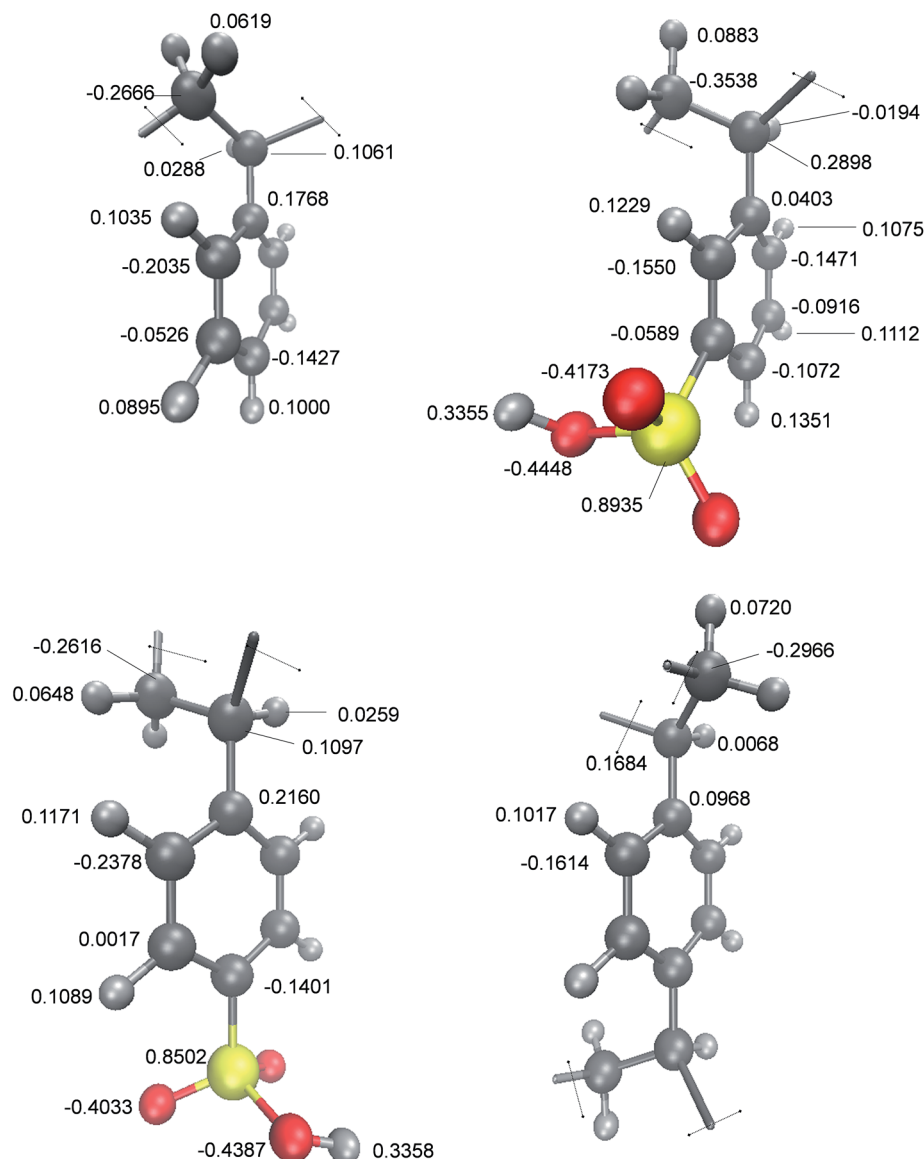


Fig. 3 Electrostatic parameters for styrene, *m*-sulfonic styrene, *p*-sulfonic styrene and divinylbenzene units.

linking procedure. Xu *et al.*⁴⁶ have also performed cross-linking simulations for epoxy resin and used their model to study the diffusion of water in these cross-linked networks.⁴⁷ The authors used an iterative MD/MM procedure to cross-link epoxy resin, where the newly formed topology is subjected to 1000 MD steps of relaxation. Heine *et al.*⁴⁸ simulated the structural and mechanical properties of large polydimethylsiloxane networks, modeled as a united atom model, using a dynamic cross-linking approach based on the cutoff distance criterion. Here, the newly formed topology was relaxed using a modified potential that was linear at large distances and quadratic at short distances. Varshney *et al.*⁴⁹ used different approaches to build highly crosslinked polymer networks, the molecular topology being relaxed by applying a multistep relaxation procedure during cross-linking.

Along with building atomistic models, simulations methods have been extensively used to study the influence of network

topology on material properties. For example, Bandyopadhyay and Odegard⁵⁰ simulated epoxy systems, demonstrating that the mechanical properties are largely influenced by the overall crosslink degree but not by the distribution of crosslink clusters in the bulk matrix. Jang *et al.*⁵¹ modeled vinyl ester resins, showing that the Young's moduli increased with increasing double bond conversions. Soni *et al.*⁵² simulated bisphenol A diglycidyl ether (DGEBA) with curing agents of different lengths, evidencing that the glass transition temperature for those resins decreased with increasing length of curing agent. Khare and Khare⁵³ created epoxy networks of DGEBA and 4,4'-diamineodiphenyl sulfone using a diffusion approach, characterizing the dependence between the epoxy conversion and the bond formation distance. Atomistic MD simulations on cross-linked poly(vinyl alcohol) evidenced that the mechanical properties and glass transitions depend on both the network topology and crosslinking density.⁵⁴ In general, a majority of

these works indicate that the properties of crosslinked materials are highly dependent on network topology; generally, an increase in the crosslink provokes an increase in the elastic modulus and glass transition temperature. In spite of this extensive literature, the relationship between the topology of highly crosslinked ion-exchange P(S-DVB) resins and their properties, especially the structural ones, remains unknown.

The HGA and CGA procedures described above were applied for the generation of more than two hundred sulfonated P(S-DVB) microstructures. The topology of these microstructures and its relationship with the density of the system is discussed in this sub-section.

Tens of microstructures were generated using the HGA method, which was applied using $m = 7$. Two systems of

different sizes were examined by considering the following numbers of styrene (N_S) and divinylbenzene (N_{DVB}) units: $\{N_S = 727; N_{DVB} = 144\}$ and $\{N_S = 1787; N_{DVB} = 356\}$. According to the imposed values of m and n , microstructures with $N_S = 727$ and 1787 were distributed in 145 and 357 small chains, respectively, of identical chemical compositions (*i.e.* each chain contains 2 divinylbenzene units, which are shared through crosslinks with another two chains, and 5 styrene units). In general, the number of sulfonic groups (N_{sulf}) was slightly lower than N_S since the steric effects precluded the sulfonation of all the styrene units (*i.e.* N_{sulf} was ~ 721 and ~ 1761 for $N_S = 727$ and 1787, respectively). The main characteristic of the microstructures obtained using the HGA method (hereafter denoted as HGA-145 and HGA-357 depending on the number of small chains) is the homogeneous distribution of the styrene and divinylbenzene units. This is evidenced in Fig. 4a, which displays one HGA-357 microstructure after MD relaxation.

Homogeneous structures derived from the HGA method systematically led to very unsatisfactory density values. This is evidenced in Fig. 5, which shows the temporal evolution of the apparent density (ρ_a) for representative HGA-145 and HGA-357 microstructures. Evidently, the ρ_a values of the relaxed structures are around $1.25\text{--}1.28\text{ g cm}^{-3}$, representing an over-estimation close to 30% with respect to the experimental value (Table 1). These high density values are due to the homogeneous topology of the resin that is motivated by our HGA algorithm. Thus, detailed topological analyses of the HGA microstructures indicates that independent of the number of small chains, all the crosslinks are identical, as schematically depicted in Fig. 6a. HGA microstructures, which do not reflect the characteristics and inhomogeneity typically associated with highly crosslinked resins, systematically fail in the reproduction of essential properties, such as the apparent density and porosity. According to these features, the rest of this work has been exclusively focused on the microstructures generated by the CGA method.

Around 150 microstructures were generated using the CGA method considering $\{N_S = 2141; N_{DVB} = 358\}$. The inspection of the topologies of the generated structures indicates that this procedure facilitates the formation not only of simple

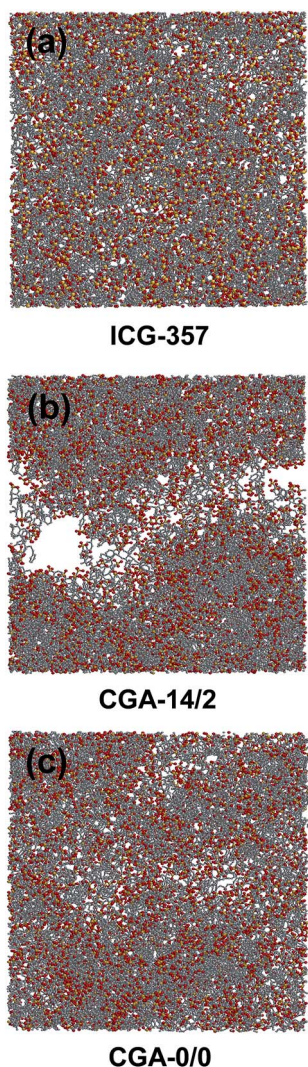


Fig. 4 Representative microstructures obtained using the (a) HGA and (b and c) CGA procedures, and subsequently relaxed with MD. The HGA microstructure depicted in (a) was generated using $\{N_S = 1787; N_{DVB} = 356\}$, while the CGA microstructures displayed in (b) and (c) were constructed using $\{N_S = 2141; N_{DVB} = 358\}$, the latter two differing in the topology. Thus, the CGA microstructure depicted in (b) involves 14 super-crosslinks and 2 inter-crosslinks (CGA-14/2), while that shown in (c) does not contain super- and inter-crosslinks (CGA-0/0).

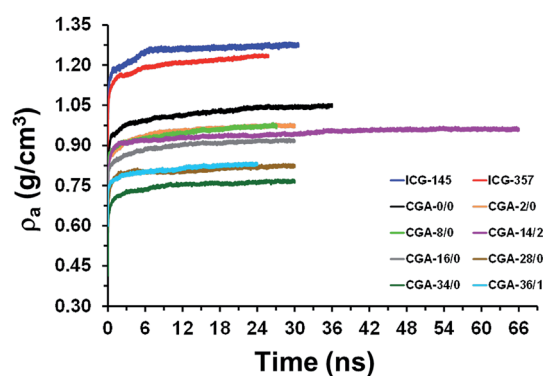


Fig. 5 Temporal evolution of the apparent density (ρ_a) during the MD relaxation process for the representative microstructures generated using the HGA and CGA methods.

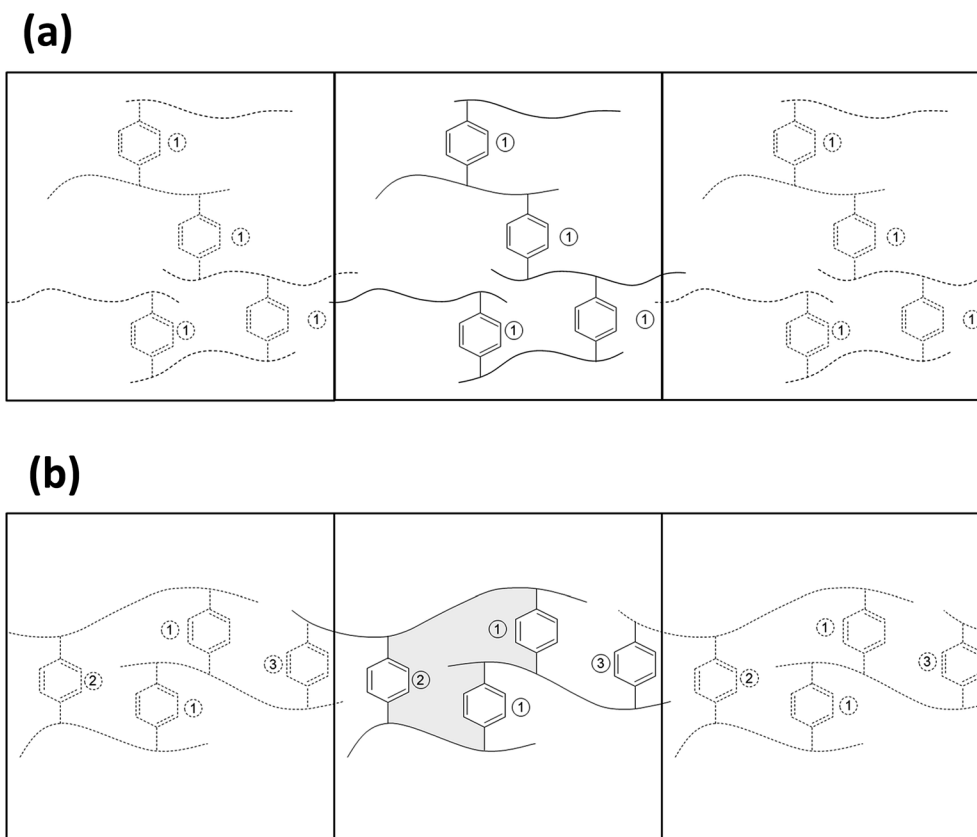


Fig. 6 (a) Simple crosslinks in microstructures generated using the HGA method. The topology of the crosslinks located at the own simulation box (center) and its images (left and right) are identical, labelled as 1. Simple crosslinks are also obtained using the CGA method. (b) Super- and inter-crosslinks in the microstructures generated using the CGA method. Super-crosslinks, which are formed by two or more crosslinks (in the image: 2 crosslinks with label 1 and one crosslink with label 2) closing a loop, define a cyclic topology (in the image: perimeter of the grey area). Inter-crosslinks (labelled as 3) connect polystyrene fragments located at the own simulation box (center) and its image (left and right).

crosslinks, like those obtained using the HGA method (Fig. 6a), but also of “*super-crosslinks*”. The name super-crosslink refers to the cyclic topology defined when the formation of two or more simple crosslinks close a loop (Fig. 6b). The total number of super-crosslinks in the generated microstructures was found to vary between 0 and 37. In addition, the CGA approach sporadically generates crosslinks that connect molecular fragments located at the own simulation box and its image, hereafter denoted as “*inter-crosslinks*”. The number of these inter-crosslinks (if any) is minimal (*i.e.* ≤ 2). The most relevant characteristic of the structures with super-crosslinks is the heterogeneity and porosity provoked by the constraints associated with the topology of the loop. This is evidenced in the representative microstructure depicted in Fig. 4b, which contains 14 super-crosslinks and 2 inter-crosslinks. In contrast, CGA microstructures in which the crosslink topology does not allow to define super-crosslinks are homogeneous and relatively similar to those obtained using the HGA method (Fig. 4c).

In order to evaluate the influence of the topology on both the density and porosity (θ), Fig. 5 represents the temporal evolution of ρ_a during the relaxation process for a selected number of CGA microstructures. These microstructures are identified using the following label code: CGA- $N_{\text{scl}}/N_{\text{inter}}$, where N_{scl} and N_{inter} correspond to the number of super-crosslinks and the

number of inter-crosslinks, respectively. Table 2 lists the main characteristics of the CGA- $N_{\text{scl}}/N_{\text{inter}}$ microstructures as well as the values of ρ_a and θ , which were averaged by considering the last 10 ns of the production runs. The value of θ was calculated using the Widom insertion method.^{55,56}

Table 2 Characteristics and properties of selected microstructures generated using the CGA strategy and relaxed using MD. Properties were averaged considering the snapshots recorded during the last 10 ps of the MD relaxation run

Label ^a	N_{scl}^b	N_{inter}^c	N_{sulf}^d	ρ_a^e (g cm ⁻³)	θ^f (%)	ρ_s^g (g cm ⁻³)
CGA-0/0	0	0	2111	1.02	16	1.22
CGA-2/0	2	0	2116	0.97	23	1.26
CGA-8/0	8	0	2110	0.94	22	1.21
CGA-16/0	16	0	2109	0.92	26	1.24
CGA-28/0	28	0	2112	0.82	32	1.22
CGA-34/0	34	0	2122	0.77	37	1.22
CGA-14/2	14	2	2120	0.96	23	1.24
CGA-36/1	36	1	2122	0.83	33	1.24

^a The code used to identify the microstructures corresponds to CGA- $N_{\text{scl}}/N_{\text{inter}}$. ^b Number of super-crosslinks. ^c Number of inter-crosslinks. ^d Number of sulfonic acid groups. ^e Apparent density. ^f Porosity. ^g Skeletal density.

The apparent density decreases with increasing N_{scl} , while, conversely, the porosity increases with N_{scl} . A comparison of the ρ_{a} values calculated for CGA- $N_{\text{scl}}/0$ microstructures with the experimental measure³⁰ ($\rho_{\text{a}} = 0.97 \text{ g cm}^{-3}$) indicates an excellent agreement for CGA-2/0 ($\rho_{\text{a}} = 0.97 \text{ g cm}^{-3}$) and a significant underestimation for CGA-34/0 ($\rho_{\text{a}} = 0.77 \text{ g cm}^{-3}$). Nevertheless, the porosity predicted for CGA-2/0 ($\theta = 22.9\%$) is lower than the experimental value ($\theta = 31.7\%$). This should be attributed to an underestimation of the pore volume per mass of resin, which was determined to be $V_{\text{g}} = 0.328 \text{ cm}^3 \text{ g}^{-1}$ by nitrogen adsorption at low temperature (Table 1). In this work, the theoretical estimations of V_{g} have been obtained using the following expression:

$$\theta = \frac{V_{\text{g}}}{V_{\text{g}} + 1/\rho_{\text{s}}} \quad (2)$$

where ρ_{s} corresponds to the skeletal density (*i.e.* that calculated using the backbone atoms only), which is included in Table 2 for the analyzed microstructures. Accordingly, V_{g} is $0.236 \text{ cm}^3 \text{ g}^{-1}$ for CGA-2/0, increasing to $0.439 \text{ cm}^3 \text{ g}^{-1}$ for CGA-34/0. The consideration of inter-crosslinks in the topology of the microstructure leads to similar results. Thus, the ρ_{a} value calculated for CGA-14/2 (0.96 g cm^{-3}) agrees with the experimental measure, while V_{g} and the porosity are slightly underestimated (*i.e.* $\sim 9\%$) by the theoretical model ($V_{\text{g}} = 0.296 \text{ cm}^3 \text{ g}^{-1}$ and $\theta = 22.8\%$).

A majority of these results suggest that there is no simple direct correlation between the topology, density and distribution of the pores in the resin. In spite of this, the agreement between the ρ_{a} , θ and V_{g} estimations calculated for the CGA-14/2 microstructure and the experimental values indicates that the coexistence of conventional, super- and inter-crosslinks provides a reasonable microscopic description of highly cross-linked P(S-DVB) resins. On the other hand, as is evidenced in Fig. 5, the MD trajectory of CGA-14/2 microstructure was enlarged to 66 ns. The variation of the density in the last 40 ns was found to be lower than 0.7%, corroborating that the microstructures are completely relaxed after 30 ns of MD.

Structural properties

Although the results discussed in the previous sub-section revealed that the relaxed CGA-14/2 model reproduces the experimental density and underestimates V_{g} and the porosity by only 10%, the structural analyses discussed in this sub-section have been focused not only on such reliable model but also on understanding the effect of super- and inter-crosslinks in the structural properties. Fig. 7 compares the distribution of the pair of backbone dihedral angles (ξ_1 and ξ_2 in Scheme 2) just after CGA generation, at the beginning of the relaxation process (5 ns MD) and the end of the relaxation (~ 30 or ~ 60 ns MD) for CGA-0/0, CGA-8/0, CGA-16/0, CGA-34/0, CGA-14/2 and CGA-36/1 microstructures. The analysis of the results indicates that despite the fact that the microstructures were generated following independent processes, the distribution of the dihedral angles (ξ_1, ξ_2) before any relaxation does not reflect the drastic differences among them. After 5 ns of MD relaxation, the initial dihedral

distributions experience important variations that are essentially provoked by the remarkable dominance of the $(\xi_1, \xi_2) = (+150^\circ, -150^\circ)$ pair. Thus, the population of the latter (ξ_1, ξ_2) pair increases in the generated microstructures from 26–29% to 43–48% in the microstructures subjected to 5 ns of MD relaxation. This increment induces significant variations in the remaining (ξ_1, ξ_2) pairs. Other (ξ_1, ξ_2) pairs with significant populations are $(+30^\circ, +90^\circ)$ and $(-30^\circ, -90^\circ)$, even though their populations decrease from 21–22% to 15–19% when the generated structures are relaxed using 5 ns of MD. Increasing the MD simulations to ~ 30 ns or even more (*i.e.* 66 ns for CGA-14/2) only provokes very small variations ($\leq 3\%$) in the populations. A majority of the results displayed in Fig. 7 indicate that the super- and inter-crosslinks do not affect the local atomic order of the polymeric chains in the resin, which is defined by the backbone dihedral angles.

Fig. 8, which represents the temporal evolution of the distribution of the ξ_1 and ξ_2 dihedral angles along the first 30 ns of simulation, shows that the conformational relaxation occurs in only ~ 2 ns for CGA-14/2. After the initial re-arrangement, no other significant conformational change occurs during the simulation, the populations remaining practically constant along the whole trajectory. An inspection of such temporal evolution for the other models (not shown) indicates that this relaxation process occurs before 5 ns in all the cases, 2–3 ns being the most frequent interval.

In spite of the fact that the topology of P(S-DVB) does not affect the short-range atomic order, the remarkable influence of N_{scl} and N_{inter} in ρ_{a} , θ and V_{g} is expected to be reflected in the medium- and long-range structural properties. Fig. 9a and b display the radial distribution function between backbone carbon atom pairs, $g_{\text{cb-cb}}(r)$, for selected generated microstructures before and after MD relaxation, respectively. For all the profiles, the first and second sharp peaks correspond to the C–C bond length and $\angle \text{C–C–C}$ bond angle, respectively. The third and fourth peaks, which are separated by only 0.6 Å, capture the different conformational states associated with the C–C–C dihedral angles. These peaks show marginal differences between the generated microstructures (Fig. 9a), while they are practically identical for all the MD relaxed microstructures (Fig. 9b). This corroborates the marginal influence of the topology in the local atomic order at the backbone discussed above.

After those four peaks, the profiles displayed in Fig. 9 present some differences, indicating that N_{scl} and N_{inter} affect the medium- and long-range order of the backbone carbon atoms. Obviously, these differences are more pronounced for the generated microstructures than for the relaxed ones, even though they are also noticeable for the latter. These results reveal that super- and inter-crosslinks affect the relative orientation of the repeat units located at the same segment, but separated by more than two units, and the relative orientation between the units located at different segments, which, in fact, are crucial for the satisfactory description of the physical properties of the resin (*i.e.* distribution and size of the pores).

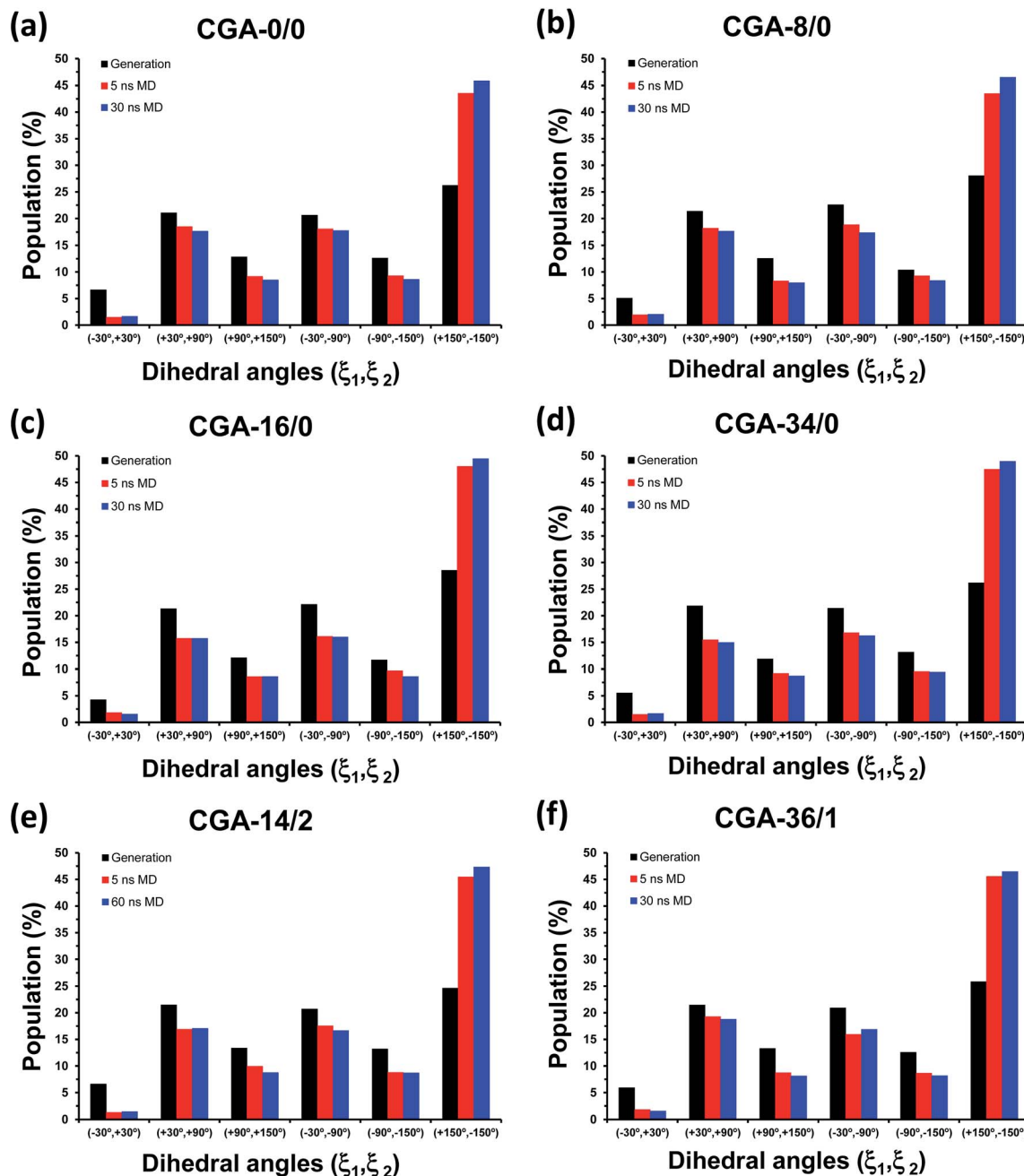


Fig. 7 Distribution of the pair of backbone dihedral angles (ξ_1, ξ_2) (Scheme 2) for selected microstructures: (a) CGA-0/0, (b) CGA-8/0, (c) CGA-16/0, (d) CGA-34/0, (e) CGA-14/2 and (f) CGA-36/1. For each case, distributions are displayed for the microstructures obtained after generation (black), after 5 ns MD relaxation (red) and after complete MD relaxation (blue).

In order to evaluate the effect of the relaxation at large distances, the internal distances between pairs of repeat units separated by L repeat units⁵⁷ were calculated for the CGA-14/2 model using the geometric centers of the aromatic ring contained in each repeat unit. Fig. 10a compares the profiles for the microstructures obtained after generation and after 66 ns of MD. The results reveal significant differences at large L values, which should be attributed to the influence of the MD relaxation on the super- and inter-crosslinks. Furthermore, a comparison of the internal distances obtained for different L values evidences Gaussian statistics in all these cases. This is

reflected in Fig. 10b, which compares the frequency of the internal distances for $L = 5, 10$ and 50 calculated using the generated and MD relaxed microstructures.

The results discussed in this sub-section and in the previous one reveal the importance of the super-crosslinks topology in the properties (*i.e.* density, porosity and structures) of highly cross-linked resins. Thus, although the inter-crosslinks ensure the local backbone structure, super-crosslinks confer rigidity and loop architecture. Thus, the length of the topological loops defined by super-crosslinks defines the pore sizes and heterogeneity in the bulk material, while the rigidity prevents the

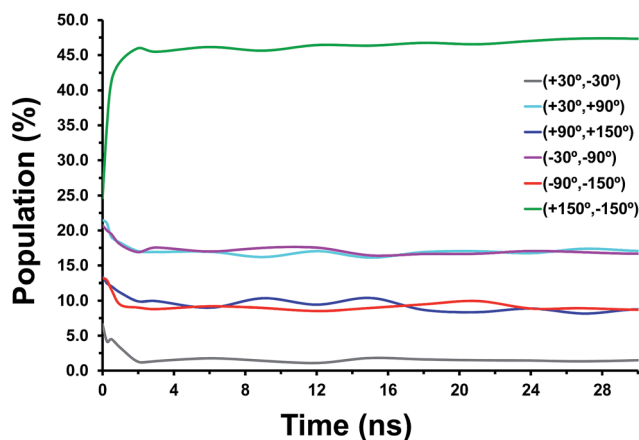
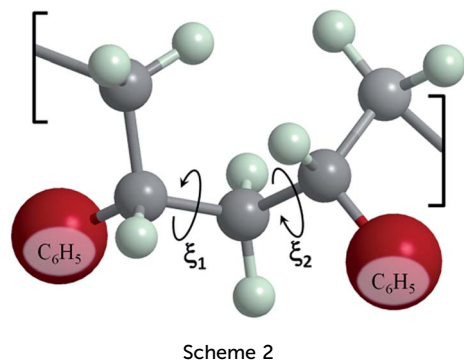


Fig. 8 Temporal evolution of the distribution of the ξ_1 and ξ_2 dihedral angles along the first 30 ns of simulation for CGA-14/2.

polymeric network collapse. Obviously, this is related with the utilization of highly cross-linked P(S-DVB) resins as a catalyst,^{13–19} since the rigid pores defined by super-crosslinks ensure high surface areas. Accordingly, the existence of super-crosslinks affects the distribution of the sulfonic groups (see below) and facilitates the swelling and accessibility to the active sites. It should be noted that the microscopic information derived from this work can be used to improve the performance of cross-linked polymeric materials, especially in the field of catalysis. This can be achieved by tailoring the topology of super-crosslinks, which, in practice, can be made simply by changing the chemical structure of the cross-linking agents.

Distribution of sulfonic groups

In order to ascertain the influence of N_{scl} and N_{inter} on the distribution of the sulfonic groups, the simulation boxes used to represent the generated and relaxed CGA microstructures were divided into 1000 identical cells. Both the sulfonation ratio, which was defined as the ratio between the number of sulfonic groups and the total number of atoms per cell, and the local apparent density were calculated for each of these cells. After this, the cells were ranked following an increasing local apparent density criterion. Fig. 11 displays the sulfonation ratio (left) and the apparent density (right) of the ranked cells for

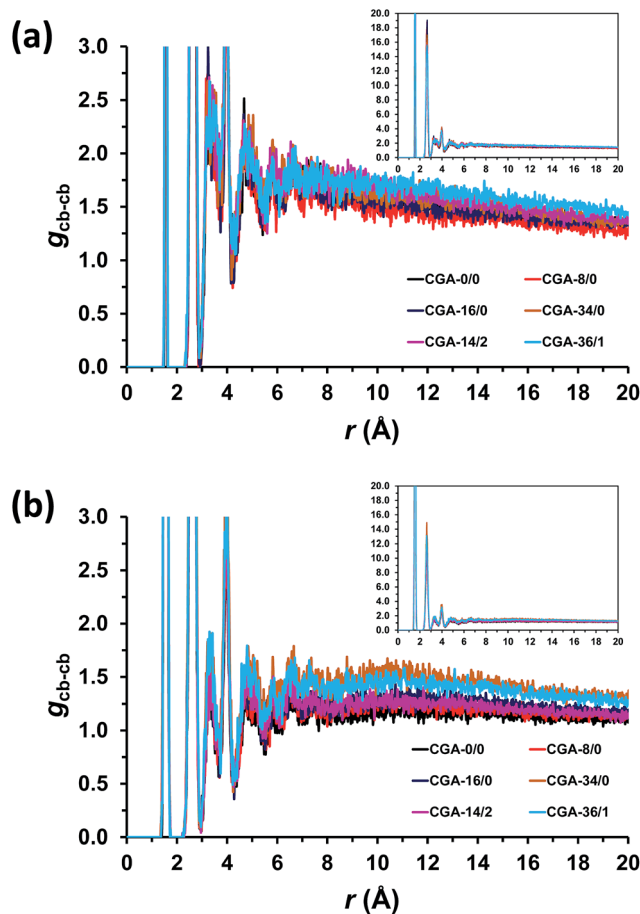


Fig. 9 Radial distribution functions of backbone carbon...backbone carbon atom pairs for selected microstructures (a) before and (b) after MD relaxation.

representative microstructures just after the generation with the CGA method and after complete MD relaxation.

The results displayed in Fig. 11 indicate that the sulfonic groups tend to be located at the regions of lower density in all the generated and relaxed microstructures, independently of N_{scl} and N_{inter} . In spite of these, important changes are detected among the different microstructures. The number of cells with negligible local apparent density values, and therefore, without sulfonic groups is higher before relaxation than after relaxation in all the cases with the exception of CGA-34/0. On the other hand, Fig. 11 reveals that MD relaxation provokes a change in the slope of the local density profile in all the cases. This change affects the number of cells (*i.e.* volumetric fraction) with local apparent densities close to the average ones (Table 2), which is noticeably higher for the relaxed microstructures. According to these observations, representations provided in Fig. 11 indicate that, in general, MD relaxation produces a homogenization of the system in terms of both sulfonic groups and local density distributions.

However, detailed analyses of these results reveal that the above mentioned homogenization affects the volume of the pores in a heterogeneous way (*i.e.* super- and inter-crosslinks enable a heterogeneous distribution of the pores). This feature

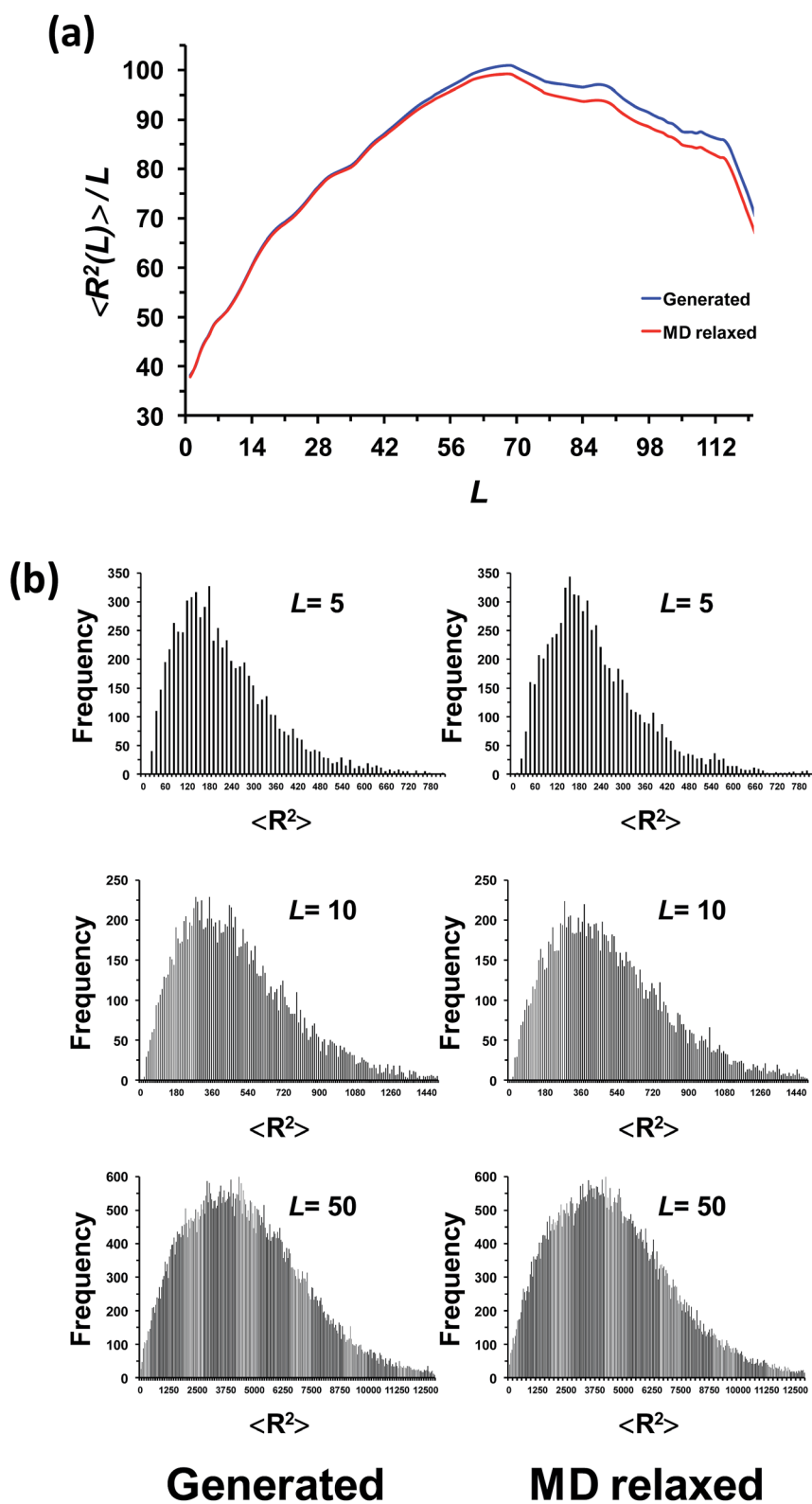


Fig. 10 (a) Internal distance distribution for the generated and MD relaxed microstructures of CGA-14/2. The internal distance, which refers to the distance between repeat units separated by L repeat units, was calculated using the geometric centers of the aromatic ring contained in each repeat unit. (b) Frequencies of the internal distance distributions considering $L = 5, 10$ and 50 for the generated (left) and MD relaxed (right) microstructures of CGA-14/2.

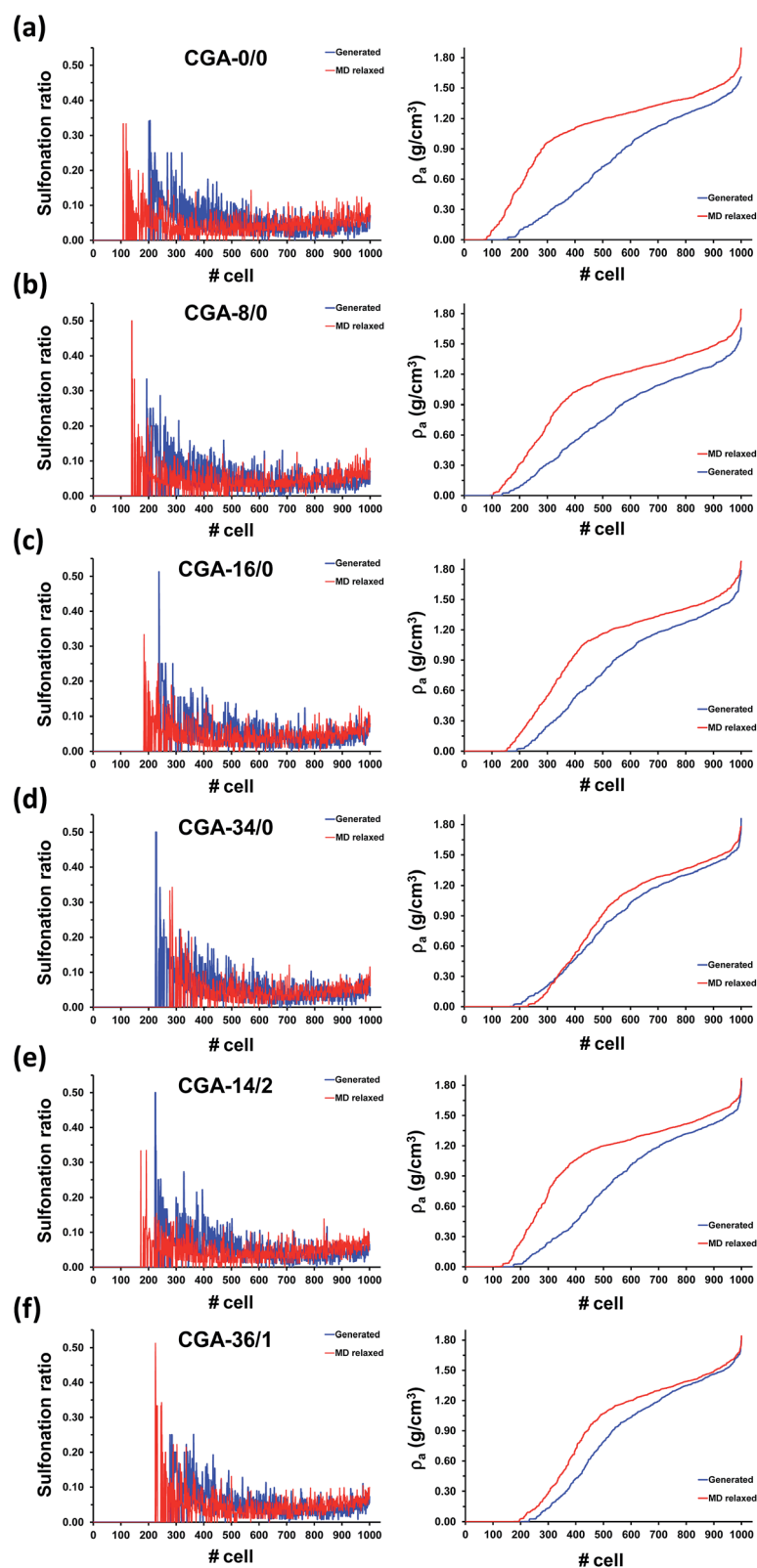


Fig. 11 Local sulfonation ratio (left) and local apparent density (right) for the 1000 cells in which each microstructure was divided for (a) CGA-0/0, (b) CGA-8/0, (c) CGA-16/0, (d) CGA-34/0, (e) CGA-14/2 and (f) CGA-36/1. Cells were ranked following a growing local density order. Profiles for microstructures before (blue) and after complete MD relaxation (red) are displayed.

is evidenced by comparing the number of cells that exhibit local densities close to the corresponding average apparent density (*i.e.* $\pm 0.05 \text{ g cm}^{-3}$) before and after MD relaxation. For example, in the absence of super-crosslinks (CGA-0/0), the number of cells with $\rho_a = 0.70 \pm 0.05 \text{ g cm}^{-3}$ is 49 in the generated microstructure, whereas in the relaxed microstructure, the number of cells with $\rho_a = 1.02 \pm 0.05 \text{ g cm}^{-3}$ is 67. This confirms that the CGA-0/0 microstructure undergoes a homogeneous re-distribution of the mass, and therefore, of the sulfonic groups upon relaxation. In contrast, after the incorporation of 8 super-crosslinks (CGA-8/0), the number of cells with $\rho_a = 0.70 \pm 0.05 \text{ g cm}^{-3}$ in the generated microstructure is smaller than the number of cells with $\rho_a = 0.94 \pm 0.05 \text{ g cm}^{-3}$ in the relaxed microstructure (*i.e.* 53 and 40, respectively). In this case, super-crosslinks preserve the volume of some pores, and the homogenization induced by the relaxation process only influences some regions. This “*heterogeneous homogenization*” also affects the distribution of sulfonic groups, the sulfonation ratio experiencing higher fluctuations in CGA-8/0 than in CGA-0/0 after MD relaxation. The heterogeneity in the homogenization process decreases with N_{scf} , as reflected by the enhanced similarity in the number of cells with apparent density close to the average value before and after relaxation (*e.g.* for CGA-16/0, the number of cells with $\rho_a = 0.72 \pm 0.05 \text{ g cm}^{-3}$ in the generated microstructure is 39, while the number of cells with $\rho_a = 0.92 \pm 0.05 \text{ g cm}^{-3}$ in the relaxed microstructure is 31). Finally, this tendency is contrary to that of CGA-34/0 in which the very low average apparent density (0.77 g cm^{-3}) is responsible for the enhanced heterogeneous distribution of sulfonic groups observed upon relaxation. Similar features are observed for CGA-14/2 and CGA-36/1, whose average apparent density and number of super-crosslinks are high enough (Table 2) to observe the *heterogeneous homogenization* provoked by the MD relaxation process. Thus, the characteristics of CGA-14/2 are similar to those described for CGA-16/0 while CGA-36/1 behaves as CGA-34/0.

Relative orientation of the phenyl rings

The interaction between aromatic phenyl rings is normally described in terms of the center of mass–center of mass partial radial distribution function, $g_{\text{p-p}}(r)$. Fig. 12a and b plot the $g_{\text{p-p}}(r)$ functions calculated for different P(S-DVB) generated microstructures before and after MD relaxation, respectively. Evidently, the peaks centered at around ~ 3.7 and ~ 7 Å appear in all the cases, evidencing the presence of different types of π - π stacking interactions between the phenyl rings of P(S-DVB). The peak at ~ 3.7 Å, which is considerably less intense than that at ~ 7 Å, has been attributed to the interactions in which the aromatic rings adopt a co-facial disposition. The frequency of this kind of interaction is practically independent of the number of crosslinks and super-crosslinks in the generated microstructures (Fig. 12a). However, after MD relaxation, the abundance of co-facial interactions increases with the number of crosslinks, as is reflected by the enhancement in the height of the peak in Fig. 12b. On the other hand, the peak at ~ 7 Å has been associated with the π - π stacking interactions in which the two aromatic rings adopt a T-shape disposition. This kind of interaction is considerably more frequent than that in which

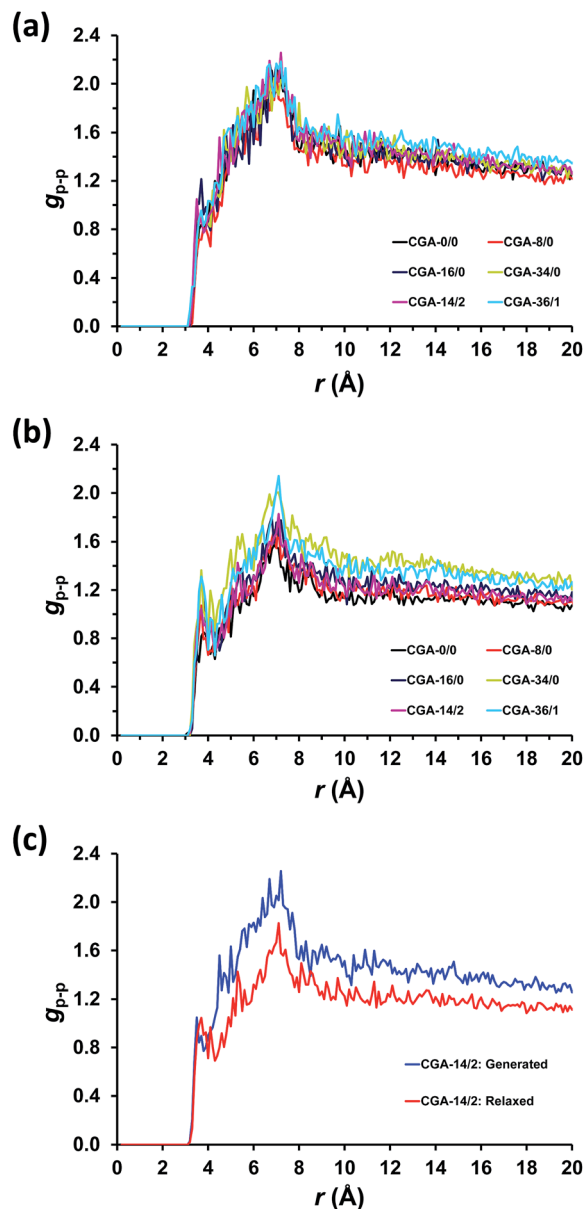


Fig. 12 Radial distribution functions of phenyl center of masses–phenyl center of masses pairs selected microstructures (a) before and (b) after MD relaxation. The profiles obtained for CGA-14/2 microstructures before and after relaxation are combined in the same figure in (c).

the two rings are co-facial. Similar to co-facial interactions, the abundance of T-shape interactions seems to be relatively independent of the number of crosslinks for the generated microstructures, whereas it increases with the number of crosslinks for relaxed microstructures. The marginal and remarkable influence of MD relaxation on the peaks at ~ 3.7 and ~ 7 Å is clearly reflected in Fig. 12c, which compares the $g_{\text{p-p}}(r)$ functions obtained for CGA-14/2 microstructures before and after relaxation.

In order to obtain greater insight into the influence of N_{scf} and N_{inter} in the relative orientation of close phenyl rings, all the pairs of phenyl rings with the centers of masses separated by a

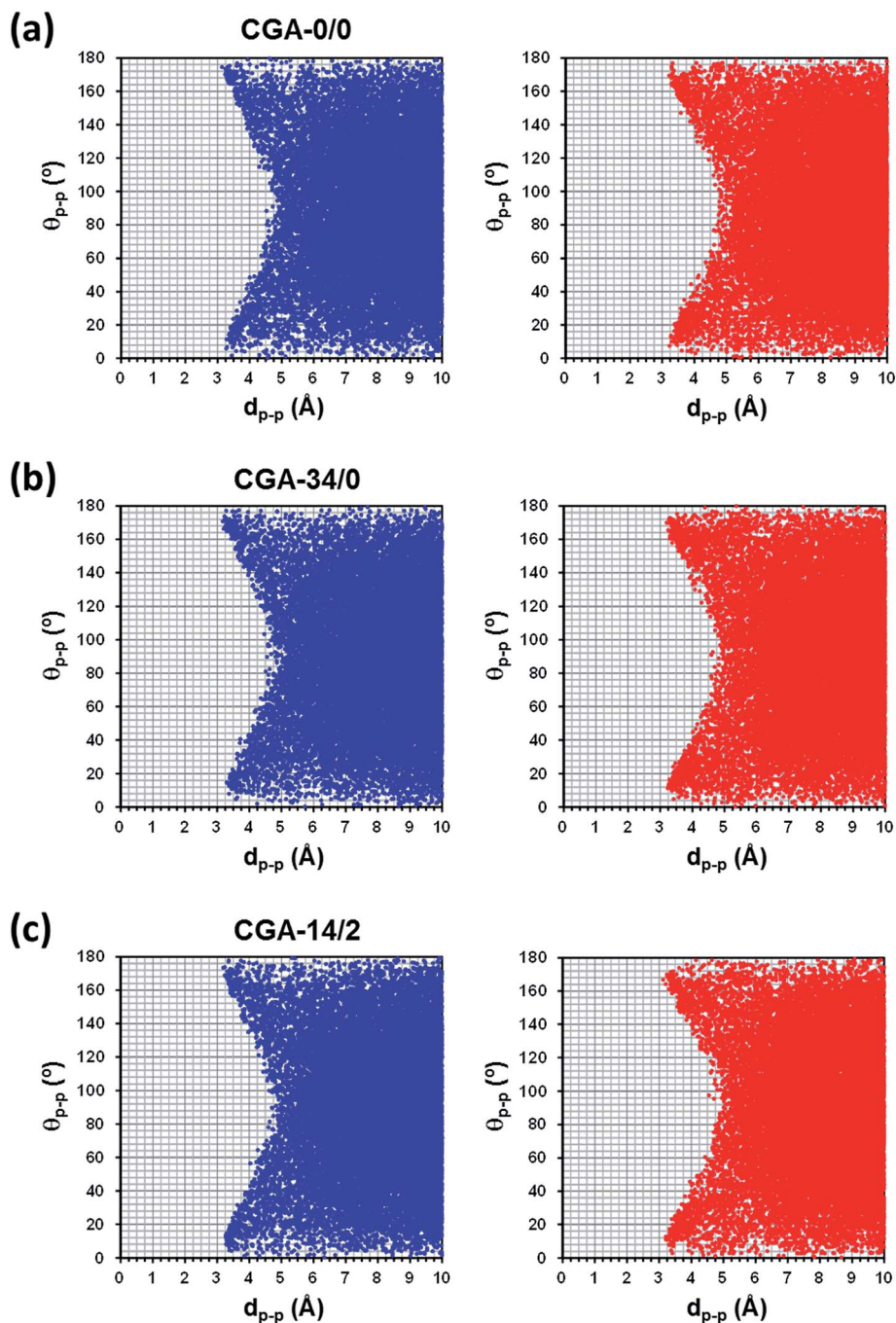


Fig. 13 Variation of d_{p-p} against θ_{p-p} for (a) CGA-0/0, (b) CGA-34/0 and (c) CGA-14/2 microstructures before (left) and after MD relaxation (right).

distance lower than 10 Å (d_{p-p}) were selected and the angle defined by their corresponding planes (θ_{p-p}) were subsequently determined. The variation of d_{p-p} against θ_{p-p} (Fig. 13) indicates that the two phenyl rings prefer a co-facial disposition when they are separated by less than ~ 5 Å, both parallel and anti-parallel configurations (*i.e.* $\theta_{p-p} \approx 0^\circ$ and 180° , respectively) being detected. However, a homogeneous distribution of θ_{p-p} is obtained for d_{p-p} values higher than ~ 5 Å, indicating that co-facial, T-shaped ($\theta_{p-p} \approx 90^\circ$) and tilted or herringbone (θ_{p-p} comprised between 30° and 60° as well as between 120° and

150°) inter-ring orientations coexist in the same microstructure. Moreover, these results, which are very similar before and after MD relaxation, are practically independent of N_{sel} and N_{inter} . The latter features are reflected in Fig. 13, which compares the results obtained for CGA-0/0, CGA-34/0 and CGA-16/2 generated and relaxed microstructures.

Modeling of P(S-DVB) resin with butanol

Finally, the preliminary investigations of butanol-containing P(S-DVB) resin were carried out to check the performance of our

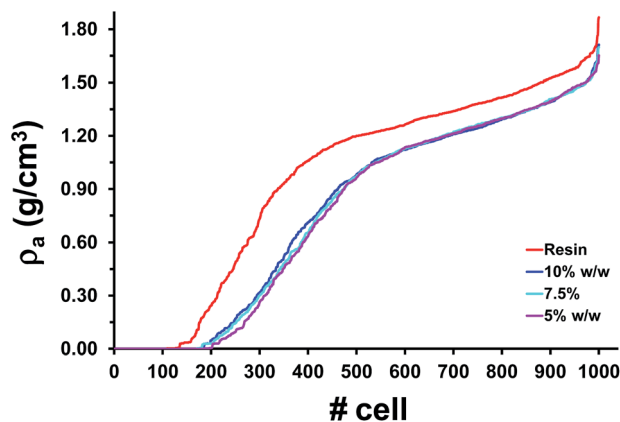


Fig. 14 Local apparent density for the 1000 cells in which each microstructure was divided for the CGA-14/2 resin without butanol and contained 5, 7.5 and 10% w/w butanol. Cells were ranked following a growing local density order.

model. MD simulations were performed considering 5, 7.5 and 10% w/w of butanol, which was modeled using the GAFF force-field³³ and RESP charges parametrized at the HF/6-311G(d,p) level,⁵⁸ combined with the CGA-14/2 model. The simulation conditions were identical to those previously described for the resin, and the production runs were of 30 ns. The apparent density, which was averaged over the last 5 ns of simulation, for the resin containing 5, 7.5 and 10% w/w butanol was of 0.96, 0.98 and 0.96 g cm⁻³, respectively. These values are practically identical to that obtained in the absence of butanol, indicating that the alcohol provokes the swelling of the resin. This swelling effect is clearly evidenced in Fig. 14, which depicts the distribution of the local apparent density calculated for the 1000 identical cells in which the simulation box was divided (*i.e.* this representation is analogous to that described above in Fig. 11). Evidently, alcohol provokes a reduction of the density in all the cells with respect to that calculated in the absence of butanol. A more detailed description of the impact of the alcohol on the structure and properties of the resin will be provided in future studies.

Conclusions

Highly crosslinked sulfonated P(S-DVB) resins have been modeled using a generation-relaxation strategy. Two different approaches have been used for the generation of initial microstructures, which have been subsequently relaxed using MD simulations. The simplest strategy, called HGA, is based on the generation of homogeneous polymeric matrices constituted by short chains of identical lengths that are connected through conventional crosslinks. This homogeneous topology, which is maintained after MD relaxation, leads to an overestimation of the density and to an underestimation of the porosity with respect to the experimental values. On the other hand, the CGA strategy combines two different algorithms that allow the heterogeneous growing and branching of the chains. This combination enables the formation of complex topological features through super- and inter-crosslinks, which are

essential for the satisfactory description of the density, porosity and pore volume of the studied P(S-DVB) resins. More specifically, the consistency between the experimental and calculated properties indicates that the topologies associated with the CGA-14/2 microstructures correspond to those of the actual systems under investigation.

Although super-crosslinks do not affect the local structural properties, the topological loops associated with them largely affect the distribution of the sulfonic group, the local distribution of the density, the medium- and long-range structural properties, and the frequency of co-facial π - π stacking interactions. Thus, the constraints associated with the topology of the super-crosslinks are responsible for the heterogeneous homogenization experienced by the generated microstructures upon MD relaxation, and consequently for the porosity typically associated with this type of membrane.

Acknowledgements

Financial support from the MICINN and FEDER (MAT2012-34498) and Generalitat de Catalunya (research group 2014 SGR 925 and XRQTC) is gratefully acknowledged. Authors are indebted to the Centre de Supercomputació de Catalunya (CESCA) for the computational resources provided. M. A. P. is grateful to financial support through a FPI grant (FPI: BES-2011-048815).

References

- 1 C. Pacurariu, G. Mihoc, A. Popa, S. G. Muntean and R. Ianos, *Chem. Eng. J.*, 2013, **222**, 218–227.
- 2 J. H. Huang, X. F. Wu, H. W. Zha, B. Yuan and S. G. Deng, *Chem. Eng. J.*, 2013, **218**, 267–275.
- 3 M. H. Eom, W. Kim, J. Lee, J. H. Cho, D. Seung, S. Park and J. H. Lee, *Ind. Eng. Chem. Res.*, 2013, **53**, 603–611.
- 4 W. Garcia-Vazquez, R. Ghalloussi, L. Dammak, C. Larchet, V. Nikonenko and D. Grande, *J. Membr. Sci.*, 2014, **452**, 104–116.
- 5 S. Sharma, M. Dinda, C. R. Sharma and P. K. Ghosh, *J. Membr. Sci.*, 2014, **459**, 122–131.
- 6 Z. W. Tang, S. F. Li, W. N. Yang and X. B. Yu, *J. Mater. Chem.*, 2012, **22**, 12752–12758.
- 7 G. Spoto, J. G. Vitillo, D. Cocina, A. Damin, F. Bonino and A. Zecchina, *Phys. Chem. Chem. Phys.*, 2007, **9**, 4992–4999.
- 8 S. Boussetta, C. Branger, A. Margaiilan, J. L. Boudenne and B. Coulomb, *React. Funct. Polym.*, 2008, **68**, 775–786.
- 9 T. Saitoh, S. Suzuki and M. Hiraide, *J. Chromatogr. A*, 2005, **1097**, 179–182.
- 10 C. W. Huck and G. K. Bonn, *Chem. Eng. Technol.*, 2005, **28**, 1457–1472.
- 11 S. Eeltink, S. Dolman, F. Detobel, G. Desmet, R. Swart and M. Ursem, *J. Sep. Sci.*, 2009, **32**, 2504–2509.
- 12 A. Vaast, L. Novakova, G. Desmet, B. de Haan, R. Swart and S. Eeltink, *J. Chromatogr. A*, 2013, **1304**, 177–182.
- 13 D. K. Mishra, A. A. Dabbawala and J. S. Hwang, *Catal. Commun.*, 2013, **41**, 52–55.

- 14 V. Parvulescu, V. Niculescu, R. Ene, A. Popa, M. Mureseanu, C. D. Ene and M. Andruh, *J. Mol. Catal. A: Chem.*, 2013, **366**, 275–281.
- 15 B. Wang and R. Weili, *Chem. Eng. Commun.*, 2012, **199**, 1236–1250.
- 16 L. Ronchin, G. Quartarone and A. Vavasori, *J. Mol. Catal. A: Chem.*, 2012, **353**, 192–203.
- 17 G. Z. Fan, C. J. Liao, T. Fang, M. Wang and G. S. Song, *Fuel Process. Technol.*, 2013, **116**, 142–148.
- 18 F. M. B. Coutinho, S. M. Rezende and B. G. Soares, *J. Appl. Polym. Sci.*, 2003, **102**, 3616–3627.
- 19 D. C. Sherrington, *Chem. Commun.*, 1998, 2275–2286.
- 20 P. Y. Chen and C. W. Hong, *Fuel Cells*, 2010, **10**, 17–25.
- 21 E. Allahyarov, P. L. Taylor and H. Lowen, *Phys. Rev. E: Stat., Nonlinear, Soft Matter Phys.*, 2010, **81**, 031805.
- 22 S. Shao, L. Yan, X. Ji and S. Zhu, *J. Chem. Phys.*, 2009, **131**, 224901.
- 23 L. Yan, X. Ji and W. Lu, *J. Phys. Chem.*, 2008, **112**, 15616–15627.
- 24 E. Allahyarov and P. L. Taylor, *J. Phys. Chem. B*, 2009, **113**, 610–617.
- 25 J. Pozuelo, E. Riande, E. Saiz and V. Compañ, *Macromolecules*, 2006, **39**, 8862–8866.
- 26 O. Bertran, D. Curcó, J. Torras, C. A. Ferreira and C. Alemán, *Macromolecules*, 2010, **43**, 10521–10527.
- 27 E. Córdova-Mateo, O. Bertran, C. A. Ferreira and C. Alemán, *J. Membr. Sci.*, 2013, **428**, 393–402.
- 28 E. Córdova-Mateo, O. Bertran and C. Alemán, *J. Phys. Chem. C*, 2014, **118**, 17643–17654.
- 29 R. Kunin, E. F. Meitzner, J. A. Oline, S. A. Fisher and N. Frisch, *Ind. Eng. Chem. Prod. Res. Dev.*, 1962, **1**, 140–144.
- 30 C. Casas, R. Bringué, E. Ramírez, M. Iborra and J. Tejero, *Appl. Catal., A*, 2011, **396**, 129–139.
- 31 S. Fisher and R. Kunnin, *J. Anal. Chem.*, 1955, **27**, 1191–1194.
- 32 C. Alemán, N. C. Karayiannis, D. Curcó, K. Foteinopoulou and M. J. Laso, *J. Mol. Struct.: THEOCHEM*, 2009, **898**, 62–72.
- 33 J. Wang, R. M. Wolf, J. W. Caldwell, P. A. Kollman and D. A. Case, *J. Comput. Chem.*, 2004, **25**, 1157–1174.
- 34 P. Cieplak, W. Cornell, C. I. Bayly and P. A. Kollman, *J. Comput. Chem.*, 1995, **16**, 1357–1377.
- 35 V. M. Anisimov, G. Lamoureux, I. V. Vorobyov, N. Huang, B. Roux and A. D. MacKerell Jr, *J. Chem. Theory Comput.*, 2005, **1**, 153–168.
- 36 I. Vorobyov, V. M. Anisimov, S. Greene, R. M. Venable, A. Moser, R. W. Pastor and A. D. MacKerell Jr, *J. Chem. Theory Comput.*, 2007, **3**, 1120–1133.
- 37 A. Toukmaji, C. Sagui, J. Board and T. Darden, *J. Chem. Phys.*, 2000, **113**, 10913–10927.
- 38 W. G. Hoover, *Phys. Rev. A*, 1985, **31**, 1695–1697.
- 39 S. Nosé, *J. Chem. Phys.*, 1984, **81**, 511–519.
- 40 M. Parrinello and A. Rahman, *J. Appl. Phys.*, 1981, **52**, 7182–7190.
- 41 D. C. Doherty, B. N. Holmes, P. Leung and R. B. Ross, *Comput. Theor. Polym. Sci.*, 1998, **8**, 169–178.
- 42 I. Yarovsky and E. Evans, *Polymer*, 2002, **43**, 963–969.
- 43 J. H. Gou, B. Minaie, B. Wang, Z. Y. Liang and C. Zhang, *Comput. Mater. Sci.*, 2004, **31**, 225–236.
- 44 H. B. Fan and M. M. F. Yuen, *Polymer*, 2007, **48**, 2174–2178.
- 45 Accelrys Inc., San Diego, CA.
- 46 C. F. Wu and W. J. Xu, *Polymer*, 2006, **47**, 6004–6009.
- 47 C. F. Wu and W. J. Xu, *Polymer*, 2007, **48**, 5440–5448.
- 48 D. R. Heine, G. S. Grest, C. D. Lorenz, M. Tsige and M. J. Stevens, *Macromolecules*, 2004, **37**, 3857–3864.
- 49 V. Varshney, S. S. Patnaik, A. K. Roy and B. L. Farmer, *Macromolecules*, 2008, **41**, 6837–6842.
- 50 A. Bandyopadhyay and G. M. Odegard, *Modell. Simul. Mater. Sci. Eng.*, 2012, **20**, 015018.
- 51 C. Jang, T. E. Lacy, S. R. Gwaltney, H. Toghiani and C. U. Pittman Jr, *Macromolecules*, 2012, **45**, 4876–4885.
- 52 N. Soni, P.-H. Lin and R. Khare, *Polymer*, 2012, **53**, 1015–1019.
- 53 K. S. Khare and R. Khare, *Macromol. Theory Simul.*, 2012, **21**, 322–327.
- 54 J. Sacristan-Bermejo and C. Mijangos-Ugarte, *Macromol. Theory Simul.*, 2009, **18**, 317–327.
- 55 B. Widom, *J. Phys. Chem.*, 1982, **86**, 869–872.
- 56 B. Widom, *J. Chem. Phys.*, 1963, **39**, 2808–2812.
- 57 V. A. Harmandaris, N. P. Adhikari, N. F. A. van der Vegt and K. Kremer, *Macromolecules*, 2006, **39**, 6708–6719.
- 58 C. Caleman, P. J. van Maaren, M. Hong, J. S. Hub, L. T. Costa and D. van der Spoel, *J. Chem. Theory Comput.*, 2012, **8**, 61–74.